

Detection of (dark) matter concentrations via weak gravitational lensing

Peter Schneider
Max-Planck-Institut für Astrophysik
Postfach 1523
D-85740 Garching, Germany

Abstract

The distortion of images of faint background galaxies by (weak) gravitational lensing can be used to measure the mass distribution of the deflector. Reconstruction methods for the mass profile of lensing clusters have been developed and successfully tested. Alternatively, the image distortions can be used to define a weighted mean of the mass inside a circular aperture, as was first suggested by Kaiser. This “aperture mass” has the advantage that strict error bars can be obtained from the data itself, and that a strict lower limit of the lens mass inside a circle can be obtained.

The aperture mass can thus be used to *detect* dark matter concentrations. Keeping in mind that wide-field cameras will become increasingly available, this method can be used to search for mass concentrations on wide-field images. To do this, the aperture mass measure is generalized to account for different weighting functions. For each such weighting function, a signal-to-noise ratio can be calculated. For an assumed mass profile of the density concentrations, the weighting function can be chosen such as to maximize the resulting signal-to-noise ratio. Assuming that dark matter halos can be approximated by an isothermal profile over a large range of radius, a weighting function is constructed which is adapted to this density profile and which yields a smooth signal-to-noise map. Numerical simulations which adopt parameters characteristic of 4-m class telescopes are then used to show that dark halos with a velocity dispersion in excess of ~ 600 km/s can be reliably detected as significant peaks in the signal-to-noise map. The effects of seeing and an anisotropic PSF are then investigated and shown to be less important than might be feared. It is thus suggested that the method of aperture mass measures developed here can be used to obtain a mass-selected sample of dark halos, in contrast to flux-selected samples. Shear fields around high-redshift bright QSOs as detected by Fort et al. provide a first successful application of this strategy. The simplicity of the method allows its routine application to wide-field images of sufficient depth and image quality.

1 Introduction

Objects in the universe are usually discovered by means of their emitted radiation – the brighter the objects are, the easier they are detected. Therefore, all samples of objects are flux limited. The inclusion of objects thus depends, among other things, on the wavelength of observation. As an example, clusters of galaxies can be selected either by X-ray surveys or from optical images. There is no reason to expect that the clusters selected by these two methods will share most of their properties; in the former case, clusters with a dense intracluster medium will be preferentially included in the samples, whereas optical survey are sensitive to clusters which contain many bright galaxies. Given that the intracluster gas and the galaxies constitute only a small fraction of the cluster mass, which is the quantity cosmologists are most interested in, it is by no means clear that flux-limited samples reveal a fair representation of (dark) matter concentrations in the universe.

Gravitational lensing offers the possibility to detect ‘unseen’ matter concentrations just from their gravitational effect on light rays. For example, the quantitative analysis of the currently existing surveys for gravitationally-lensed QSOs can rule out a significant density of compact lenses in the universe with mass $\gtrsim 10^{11} M_\odot$ (e.g., Kochanek 1993, 1995; Maoz & Rix 1993). Constraints from QSO variability and spectral characteristics have yielded strict upper limits on the cosmological density of compact objects with $10^{-3} M_\odot \lesssim M \lesssim 10^2 M_\odot$ (e.g., Schneider 1993; Dalcanton et al. 1994). Since most groups and clusters of galaxies are expected not to be sufficiently compact to yield multiply-imaged QSO images, these surveys do not yield significant constraints on their cosmic number density.

On the other hand, the mass distribution in clusters can be investigated with gravitational lensing, either from studying arcs and arclets (see the recent review by Fort & Mellier 1994), or from the ‘weak’ distortion of numerous faint background galaxies by the tidal gravitational field of the cluster (Tyson, Valdes & Wenk 1990; Kaiser & Squires 1993). These techniques have already yielded most interesting results; e.g., the core radius of the dark matter in clusters was found to be considerably smaller than that normally concluded from X-ray studies (e.g., Miralda-Escudé & Babul 1995 and references therein), and the mass-to-light ratio in the cluster MS1224 was found to be considerably larger than ‘typical’ estimates in other clusters (Fahlman et al. 1994). This object supports the possibility that clusters of rather different mass-to-light ratios exist, and that optical survey are (strongly) biased towards the detection of only the brightest subset of these clusters.

These lensing studies of clusters have been performed exclusively on clusters which were known before from optical or X-ray surveys. However, Fort et al. (1996) have recently started to develop a strategy for the detection of mass concentrations which are not included in existing samples. Supported by the findings that there is a statistically significant overdensity of (foreground) galaxies and clusters around high-redshift bright QSOs (Fugmann 1990; Bartelmann & Schneider 1993, 1994; Rodrigues-Williams & Hogan 1994; Benitez & Martinez-Gonzalez 1995; Hutchings 1995; Seitz & Schneider 1995b), on scales in excess of several arcminutes, they assumed that these apparently most luminous QSOs are affected by the magnification bias. This magnification cannot be due to single galaxies, as the relevant scale in this case would be of order arcseconds, but must come from more extended mass concentrations. Fort et al. (1996) have tried to

discover the presence of (foreground) mass concentrations, i.e., by mapping the (weak) shear in the field of the QSO, by investigating the systematic ellipticity component of background galaxies. In several of the fields which they imaged, a significant shear field was detected, which provides a direct verification of the overdensity of material near the line-of-sight to these QSOs. One might suspect that in this way, one could obtain a ‘mass-selected’ sample of groups and/or clusters of galaxies.

The main drawback of this method is that high-redshift, bright QSOs are rare, and these mass concentrations are selected only along these rare lines-of-sight. On the other hand, several wide-field imaging cameras are either installed or planned, and the resulting images can be used to systematically search for dark matter concentrations. In this paper, a statistical method for the detection of (dark) matter concentrations is described which is also based on weak lensing of background galaxies. From the image ellipticities of background galaxies, one can derive a shear map, and from that, the surface mass density of the lens can be reconstructed (Kaiser & Squires 1993; Schneider & Seitz 1995; Seitz & Schneider 1995a, 1996b; Bartelmann et al. 1996). One could then analyze the resulting mass maps to search for matter concentrations. However, the relation between galaxy ellipticities and the resulting mass map is quite complicated, and no simple test for a statistical significance of a concentration has been derived yet (although numerical simulations can in principle derive such significance levels). Alternatively, Kaiser (1995) pointed out that the mean surface mass density in a circular aperture can be directly obtained from the shear,

$$\zeta(x_1, x_2) := \bar{\kappa}(x_1) - \bar{\kappa}(x_1, x_2) = \frac{2x_2^2}{x_2^2 - x_1^2} \int_{x_1}^{x_2} \frac{dx}{x} \langle \gamma_t \rangle(x) \quad , \quad (1)$$

where $\bar{\kappa}(x_1)$ is the mean dimensionless surface mass density within a circle of radius x_1 around a point, $\bar{\kappa}(x_1, x_2)$ is the mean dimensionless surface mass density in an annulus of radii x_1 and $x_2 > x_1$ around the same point, and $\langle \gamma_t \rangle(x)$ is the mean tangential component of the shear at distance x from that reference point. Given that κ is non-negative, the above relation can be used to put a rigorous lower bound on the mass contained inside the circle of radius x_1 around the reference point.

In this paper, the relation (1) is first generalized to allow for arbitrary weight functions. If one assumes that the mass concentrations one expects to detect have an approximately isothermal profile over a significant fraction of their extent, the weight function can be optimized for the detection of such objects. The important point to note then is that these aperture measures have well-defined and simple statistical properties. This allows to generate a signal-to-noise map from the ellipticities of the faint galaxies, in which sufficiently strong lenses will appear as significant (say, $\gtrsim 4\sigma$) peaks. This method is then tested on synthetically generated data sets, and it is shown that it lives up to the expectation. In particular, the signal-to-noise map is not corrupted by small-scale deflectors (such as individual galaxies), nor by larger-scale deflectors. Perhaps most importantly, the signal-to-noise maps are much more weakly affected by seeing and an anisotropic point-spread function than one might fear, at least as long as the PSF is fairly stable over the ‘filter scale’. As will be shown in Sect. 4, ‘isothermal’ mass concentrations with a velocity dispersion in excess of ~ 600 km/s can be reliably detected by our new method, where this lower limit depends on the seeing and the depth of the observations. We therefore conclude that this detection method, which is very easy to implement numer-

ically and which is fast, can be used routinely on wide-field images to search for dark mass concentrations.

After the work for this paper was completed, a paper by Squires & Kaiser (1996) was distributed as a preprint. They have also generalized the aperture densitometry (1) to arbitrary weight functions. Our result (15) agrees with theirs.

2 Generalized aperture densitometry

2.1 Notation

The dimensionless surface mass density $\kappa(\mathbf{x})$ as a function of angular position $\boldsymbol{\theta}$ is related to the physical surface mass density $\Sigma(\boldsymbol{\theta})$ by

$$\kappa(\mathbf{x}) = \frac{\Sigma(\mathbf{x})}{\Sigma_{\text{cr}}} \quad , \quad (2a)$$

with the critical surface mass density

$$\Sigma_{\text{cr}} = \frac{c^2 D_s}{4\pi G D_{\text{d}} D_{\text{ds}}} \quad , \quad (2b)$$

where the D 's denote the distances to the lens and source, and from the lens to the source (we use the same notation as in Schneider, Ehlers & Falco 1992). κ is related to the deflection potential $\psi(\mathbf{x})$ by a Poisson-like equation,

$$\nabla^2 \psi = 2\kappa \quad , \quad (3a)$$

or

$$\psi(\mathbf{x}) = \frac{1}{\pi} \int_{\mathbb{R}^2} d^2 x' \kappa(\mathbf{x}') \ln(|\mathbf{x} - \mathbf{x}'|) \quad . \quad (3b)$$

The shear γ is a two-component quantity which describes the traceless part of the Hessian of ψ ; in particular, we write the shear as a complex number $\gamma = \gamma_1 + i\gamma_2$, with

$$\gamma_1 = \frac{1}{2} (\psi_{11} - \psi_{22}) \quad , \quad \gamma_2 = \psi_{12} \quad , \quad (4)$$

where the indices on ψ denote partial derivatives with respect to x_i . Combining (3) and (4), one finds that

$$\gamma(\mathbf{x}) = \frac{1}{\pi} \int_{\mathbb{R}^2} d^2 x' \mathcal{D}(\mathbf{x} - \mathbf{x}') \kappa(\mathbf{x}') \quad , \quad (5)$$

where the complex kernel \mathcal{D} is given by

$$\mathcal{D}(\mathbf{x}) = -\frac{x_1^2 - x_2^2 + 2ix_1x_2}{|\mathbf{x}|^4} \quad . \quad (6)$$

If we write the vector \mathbf{x} as a complex number $X := x_1 + ix_2$, then

$$\mathcal{D}(\mathbf{x}) = \frac{-1}{(X^*)^2} \quad , \quad (7)$$

where the asterisk denotes complex conjugation. As was shown by Kaiser & Squires (1993), the relation (5) can be inverted to yield

$$\kappa(\mathbf{x}) = \frac{1}{\pi} \mathcal{R}\text{e} \left[\int_{\mathbb{R}^2} d^2x' \mathcal{D}^*(\mathbf{x} - \mathbf{x}') \gamma(\mathbf{x}') \right] + \kappa_0 \quad , \quad (8)$$

where κ_0 is an arbitrary constant, and $\mathcal{R}\text{e}(X)$ denotes the real part of the complex number X . Hence, the surface mass density can be determined from the shear field, up to an overall additive constant.

2.2 Aperture measures

Consider a point \mathbf{x}_0 and a weight function $w(x)$. We then define the quantity

$$m(\mathbf{x}_0) := \int d^2x \kappa(\mathbf{x}) w(|\mathbf{x} - \mathbf{x}_0|) = \int d^2x \kappa(\mathbf{x} + \mathbf{x}_0) w(|\mathbf{x}|) \quad , \quad (9)$$

which is the integral of κ in a circular aperture around \mathbf{x}_0 , weighted by the function w . Inserting (8), one finds

$$m(\mathbf{x}_0) = \frac{1}{\pi} \mathcal{R}\text{e} \left[\int_{\mathbb{R}^2} d^2x' \gamma(\mathbf{x}') \int d^2x \mathcal{D}^*(\mathbf{x} + \mathbf{x}_0 - \mathbf{x}') w(|\mathbf{x}|) \right] + \int d^2x \kappa_0 w(|\mathbf{x}|) \quad . \quad (10)$$

The quantity m does not depend on the undetermined constant κ_0 if one requires that

$$\int dx x w(x) = 0 \quad . \quad (11)$$

Then, by changing variables in (10) to $\mathbf{y} = \mathbf{x}' - \mathbf{x}_0$, and inserting the definition (7) of \mathcal{D} , one obtains

$$m(\mathbf{x}_0) = \frac{-1}{\pi} \mathcal{R}\text{e} \left[\int_{\mathbb{R}^2} d^2y \gamma(\mathbf{y} + \mathbf{x}_0) \int_0^\infty dx x w(x) \int_0^{2\pi} \frac{d\varphi}{(X - Y)^2} \right] \quad , \quad (12)$$

where we have again used capital letters to denote complex number, i.e., $Y = y_1 + iy_2$. The final integral in (12) can be evaluated by substituting $X = xe^{i\varphi}$, so that $d\varphi = -i dX/X$, and the integral is transformed into a loop integral. The resulting integrand then has two poles, one at $X = 0$, and one at $X = Y$. Depending on whether $x < |Y|$ or not, the second pole lies inside or outside the loop. Application of the residue theorem then yields

$$\int_0^{2\pi} \frac{d\varphi}{(X - Y)^2} = \frac{\pi}{Y^2} [2H(|X| - |Y|) - |Y| \delta(|X| - |Y|)] \quad , \quad (13)$$

where $H(x)$ is the Heaviside step function, and $\delta(x)$ is Dirac's delta 'function'. Defining the *tangential shear* $\gamma_t(\mathbf{y}; \mathbf{x}_0)$ at position \mathbf{y} relative to the point \mathbf{x}_0 by

$$\frac{\gamma_t(\mathbf{y}; \mathbf{x}_0)}{|Y|^2} = -\mathcal{R}\text{e} \left(\frac{\gamma(\mathbf{y} + \mathbf{x}_0)}{Y^2} \right) \quad , \quad (14)$$

one obtains from combining (12)–(14)

$$m(\mathbf{x}_0) = \int d^2y \frac{\gamma_t(\mathbf{y}; \mathbf{x}_0)}{|\mathbf{y}|^2} Q(|\mathbf{y}|) \quad , \quad (15)$$

where we have defined

$$Q(x) := 2 \int_0^x dx x w(x) - x^2 w(x) \quad . \quad (16)$$

Equation (15) is the main result of this section; it states that the w -weighted integral of the surface mass density can be expressed as an integral over the tangential shear, weighted by the function Q . To see the usefulness of this relation, consider the case that $w(x)$ is chosen such that

$$w(x) = 0 \quad \text{for } x > R \quad ; \quad (17)$$

then, owing to the condition (11), $Q(x) = 0$ for $x > R$. Thus, in this case, the quantity $m(\mathbf{x}_0)$ can be expressed as an integral of the tangential shear *over a finite circle* around \mathbf{x}_0 . Furthermore, if $w(x)$ is chosen such that $w(x) = \text{const.}$ for $x \leq x_1 < R$, then $Q(x) = 0$ for $x \leq x_1$. Therefore, $m(\mathbf{x}_0)$ can then be expressed as an integral of the tangential shear over the annulus $x_1 \leq |\mathbf{x} - \mathbf{x}_0| \leq R$. The ζ -statistics (1) derived by Kaiser (1995) is a special case (15), which is obtained by setting $w = \hat{w}_K$, with (setting $x_2 = R$)

$$\begin{aligned} \hat{w}_K(x) &= \frac{1}{\pi x_1^2} \quad \text{for } 0 \leq x < x_1 , \\ \hat{w}_K(x) &= \frac{-1}{\pi(R^2 - x_1^2)} \quad \text{for } x_1 \leq x < R , \\ \hat{w}_K(x) &= 0 \quad \text{for } x \geq R \quad . \end{aligned} \quad (18)$$

The obvious advantage of the ζ -statistics (1) is that it can be used to directly infer a lower bound on the mass inside a circle of radius x_1 around a point \mathbf{x}_0 , due to the non-negativity of the surface mass density, i.e., $\bar{\kappa}(x_1, x_2) \geq 0$. The reason why we are interested in the generalized aperture mass measure m is that the weight function w can be adjusted such that the m -statistics is ‘optimized’ for the detection of mass overdensities, as will be shown in the next section.

3 Signal-to-noise statistics

The observational estimate of the shear field γ proceeds by investigating the distortion of the images of faint background galaxies. Using the same notation as in Schneider & Seitz (1995) and Schneider (1995), except that here we have defined the sign of γ differently as in the quoted papers, we denote by $\epsilon^{(s)}$ the complex ellipticity of a source, such that for an elliptical source with axis ratio $r \leq 1$, $|\epsilon^{(s)}| = (1 - r)/(1 + r)$, and the phase of $\epsilon^{(s)}$ is twice the angle between the major axis and the positive x_1 -direction (see also Sect. 4.4 below). The (complex) image ellipticity ϵ is obtained from $\epsilon^{(s)}$ and the local lens parameters as

$$\epsilon = \frac{\epsilon^{(s)} + g}{1 + g^* \epsilon^{(s)}} \quad , \quad (19)$$

where $g = \gamma/(1 - \kappa)$ is the (complex) *reduced shear*.¹ In the case of weak lensing, which should mainly be considered here, $g \approx \gamma$. Assuming that the intrinsic orientation of the sources is random, then the expectation value of the average ellipticity of a local sample of galaxy images becomes (see Schramm & Kayser 1995; Seitz & Schneider 1996a)

$$\langle \epsilon \rangle_\epsilon = g \approx \gamma . \quad (20)$$

Thus, the ellipticity of a galaxy image is an unbiased estimate of the local shear in the case of weak lensing.

Let n be the number density of galaxy images, and let \mathbf{x}_i and ϵ_i denote the position vectors and ellipticities of the galaxies. Defining in analogy to (14) the *tangential ellipticity* $\epsilon_{ti}(\mathbf{x}_0)$ of galaxy image i relative to the point \mathbf{x}_0 by

$$\epsilon_{ti}(\mathbf{x}_0) = -\mathcal{R}\text{e} \left(\frac{\epsilon_i(\mathbf{X}_i - \mathbf{X}_0)^*}{(\mathbf{X}_i - \mathbf{X}_0)} \right) , \quad (21)$$

where again complex number representation of the vectors \mathbf{x}_i and \mathbf{x}_0 was used on the right-hand-side, we can write down a discrete version of (15) as

$$m(\mathbf{x}_0) = \frac{1}{n} \sum_i \frac{\epsilon_{ti}(\mathbf{x}_0)}{|\mathbf{x}_i - \mathbf{x}_0|^2} Q(|\mathbf{x}_i - \mathbf{x}_0|) , \quad (22)$$

where the sum extends over all galaxy images within the aperture, i.e., within the region where $Q \neq 0$.

In the case of no lensing, the expectation value of m vanishes, $\langle m \rangle_\epsilon = 0$, because the expectation value of the tangential ellipticity is zero. The dispersion σ_{md} of m can be calculated by squaring (22) and taking the expectation value, which leads to

$$\sigma_{md}^2(\mathbf{x}_0) = \frac{\sigma_\epsilon^2}{2n^2} \sum_i \frac{Q^2(|\mathbf{x}_i - \mathbf{x}_0|)}{|\mathbf{x}_i - \mathbf{x}_0|^4} , \quad (23)$$

where the fact was used that the expectation value of the product of tangential ellipticities of different images vanishes, $\langle \epsilon_{ti} \epsilon_{tj} \rangle = 0$ for $i \neq j$, since the orientation of galaxy images are assumed to be mutually unrelated; σ_ϵ is the dispersion of the intrinsic ellipticity distribution, $\langle |\epsilon|^2 \rangle = \langle |\epsilon^s|^2 \rangle = \sigma_\epsilon^2$, and the factor 1/2 is due to the fact that the dispersion in one component of the ellipticity is $1/\sqrt{2}$ times the dispersion of the complex ellipticity, $\langle \epsilon_{ti} \epsilon_{ti} \rangle = \sigma_\epsilon^2/2$. Thus, we can define the *signal-to-noise ratio* S at position \mathbf{x}_0 as

$$S(\mathbf{x}_0) = \frac{\sqrt{2} \sum_i \frac{\epsilon_{ti}(\mathbf{x}_0)}{|\mathbf{x}_i - \mathbf{x}_0|^2} Q(|\mathbf{x}_i - \mathbf{x}_0|)}{\sqrt{\sum_i \frac{Q^2(|\mathbf{x}_i - \mathbf{x}_0|)}{|\mathbf{x}_i - \mathbf{x}_0|^4}}} . \quad (24)$$

Note that S is independent of the normalization of Q , and thus the normalization of w .

Up to now the weight function $w(x)$, and thus $Q(x)$, has been undetermined. We shall now derive the shape of $w(x)$ which maximizes the signal-to-noise ratio for a given

¹ The transformation (19) is valid only if $|g| < 1$; if $|g| \geq 1$, a different transformation applies (see Seitz & Schneider 1996a). However, in this paper we shall concentrate mainly on non-critical lenses, for which (19) is valid.

mass profile. In order to simplify the notation, we set $\mathbf{x}_0 = \mathbf{0}$ in the following consideration. The expectation value of m is

$$\langle m \rangle_d = \frac{1}{n} \sum_i \frac{\gamma_t(\mathbf{x}_i)}{|\mathbf{x}_i|^2} Q(|\mathbf{x}_i|) \quad . \quad (25)$$

Assuming that $w(x) = 0$ for $x > R$, so that $Q(x) = 0$ for $x > R$ (we shall call R the ‘aperture size’, or the ‘filter scale’), we can perform an ensemble average by averaging (25) over the probability distribution for the galaxy positions,

$$\langle m \rangle_c = \left[\prod_{k=1}^N \int \frac{d^2 x_k}{\pi R^2} \right] \langle m \rangle_d = 2\pi \int_0^R dx x \langle \gamma_t \rangle(x) \frac{Q(x)}{x^2}, \quad (26)$$

where N is the expected number of galaxies within R , $N = n\pi R^2$, and $\langle \gamma_t \rangle(x)$ is the mean tangential shear on a circle of radius x around the point $\mathbf{x}_0 = \mathbf{0}$. The indices ‘c’ and ‘d’ stand for continuous and discrete. Accordingly, we can perform a similar ensemble average of the dispersion (23), to obtain

$$\sigma_{mc}^2 = \left[\prod_{k=1}^N \int \frac{d^2 x_k}{\pi R^2} \right] \sigma_{md}^2 = \frac{\pi \sigma_\epsilon^2}{n} \int_0^R dx \frac{Q^2(x)}{x^3} \quad . \quad (27)$$

From (26) and (27) one can define the ensemble-averaged signal-to-noise ratio S_c as

$$S_c = \frac{2\sqrt{\pi n}}{\sigma_\epsilon} \frac{\int_0^R dx \langle \gamma_t \rangle(x) Q(x)/x}{\sqrt{\int_0^R dx Q^2(x)/x^3}} \quad . \quad (28)$$

According to the Cauchy–Schwarz inequality,

$$\left(\int dx f(x) g(x) \right)^2 \leq \left(\int dx f^2(x) \right) \left(\int dx g^2(x) \right) \quad ,$$

with equality if and only if $f/g = \text{const.}$, one sees by identifying $f = Q/x^{3/2}$ and $fg = \langle \gamma_t \rangle Q/x$ that S_c^2 is maximized if

$$Q(x) \propto x^2 \langle \gamma_t \rangle(x) \quad . \quad (29)$$

The corresponding weight function $w(x)$ can be obtained by differentiation of (16), which yields a first-order ordinary differential equation for w ; the integration constant is fixed by the requirement (11). The result is

$$w(x) = 2 \int_x^R dy \frac{\langle \gamma_t \rangle(y)}{y} - \langle \gamma_t \rangle(x) \quad . \quad (30)$$

The result (30) for the weight function w which maximizes the signal-to-noise ratio for a given functional form of $\langle \gamma_t \rangle(y)$ can be written in a more suggestive form. For that, we use the fact that

$$\bar{\kappa}(y) - \langle \kappa \rangle(y) = \langle \gamma_t \rangle(y) \quad (31)$$

(see Bartelmann 1995). Here, $\bar{\kappa}(y)$ is the mean mass density within a circle of radius y , and $\langle \kappa \rangle(y)$ is the mean mass density on the circle with radius y . We can actually obtain

this result, which is trivially valid for axially-symmetric mass distributions, by setting $w(x) = H(y - x)/(\pi y^2) - \delta(x - y)/(2\pi y)$ in (9). Then, m becomes the left-hand-side of Eq. (31), whereas by inserting the corresponding function Q into (15), the right-hand-side of (31) is obtained. Using that

$$\bar{\kappa}(x) = \frac{2}{x^2} \int_0^x dx' x' \langle \kappa \rangle (x') ,$$

one finds that

$$\int_y^R dx \frac{\langle \gamma_t \rangle (x)}{x} = \int_y^R dx \frac{2}{x^3} \int_0^x dz z \langle \kappa \rangle (z) - \int_y^R dx \frac{\langle \kappa \rangle (x)}{x} .$$

After interchanging the order of integration, one finds from (30) after a short calculation that

$$w(x) = \langle \kappa \rangle (x) - \bar{\kappa}(R) . \quad (32)$$

Correspondingly, one obtains, either from (32) and (16), or from (29) and (31), that

$$Q(x) = x^2 [\bar{\kappa}(x) - \langle \kappa \rangle (y)] . \quad (33)$$

Whereas this ‘optimal’ weight function maximizes the signal-to-noise ratio, and should therefore be best suited for the purpose of this paper, it is not practical to use it, for two reasons: first, the mass profile of density inhomogeneities is not known a priori, and thus the optimal weight function cannot be determined. Secondly, the weight function is neither smooth nor continuous at $x = R$, and therefore the S statistics will not be a continuous function of position \mathbf{x}_0 . Since we want to search for significant peaks in the S -function to identify mass inhomogeneities, this non-continuous weight function will cause patterns in this map which are difficult to interpret. We shall come back to this point.

Table 1. For the weight function w as given in (34), the parameter α , b , and c are given for several combinations of ν_1 and ν_2 . In addition, $100G$ is given, where $G = R^{-2} \int_0^R dy y^{-3} Q^2(y)$

ν_1	ν_2	α	$b(\nu_2 - 1)^3$	c	100 G
0.05	0.80	0.7133	0.1511	0.1239	0.7574
0.05	0.85	0.7818	0.1450	0.1203	0.7667
0.05	0.90	0.8528	0.1398	0.1170	0.7758
0.05	0.95	0.9256	0.1351	0.1138	0.7845
0.10	0.80	0.7148	0.3596	0.2555	2.4449
0.10	0.85	0.7825	0.3435	0.2483	2.4844
0.10	0.90	0.8531	0.3298	0.2415	2.5223
0.10	0.95	0.9257	0.3180	0.2351	2.5588
0.15	0.80	0.7171	0.6251	0.3844	4.8258
0.15	0.85	0.7837	0.5941	0.3740	4.9213
0.15	0.90	0.8535	0.5682	0.3642	5.0125
0.15	0.95	0.9258	0.5461	0.3549	5.0997
0.20	0.80	0.7201	0.9544	0.5050	7.8277
0.20	0.85	0.7851	0.9022	0.4922	8.0142
0.20	0.90	0.8541	0.8593	0.4800	8.1912
0.20	0.95	0.9259	0.8232	0.4684	8.3591

Nevertheless, the optimal weight function should provide a guide for constructing weight functions which give rise to a smooth S -map. As for the weight function (18) used by Kaiser (1995), we want to have that $Q(x) = 0$ for $x \leq x_1 =: \nu_1 R$ – for example, if the mass overdensity is associated with bright galaxies, there will be no faint galaxies visible in the very inner part. This implies that $w(x) = \text{const.}$ for $x \leq \nu_1 R$. Second, since one might expect that many of the mass inhomogeneities will have approximately an isothermal profile, corresponding to $\langle \kappa \rangle(x) \propto 1/x$, the weight function should behave like $1/x - \text{const.}$ over a large interval. Third, in order to obtain a smooth function $S(\mathbf{x}_0)$, $w(x)$ should go to zero at $x = R$. The following form for $w(x)$ is suggested:

$$\begin{aligned} w(x) &= 1 \quad \text{for } x \in [0, \nu_1 R], \\ w(x) &= \frac{1}{1-c} \left(\frac{\nu_1 R}{\sqrt{(x - \nu_1 R)^2 + (\nu_1 R)^2}} - c \right) \quad \text{for } x \in [\nu_1 R, \nu_2 R], \\ w(x) &= \frac{b}{R^3} (R - x)^2 (x - \alpha R) \quad \text{for } x \in [\nu_2 R, R], \end{aligned} \quad (34)$$

where the constants α , b and c are determined from requiring continuity and smoothness (i.e., continuous first derivative) at $x = \nu_2 R$, and by the normalization constraint (11). Whereas these constants can be calculated analytically, the resulting formulae are not very enlightening. For several combinations of ν_1 and ν_2 , they are tabulated in Table 1. The function $w(x)$ is plotted for four different combinations of ν_1 and ν_2 in Fig. 1.

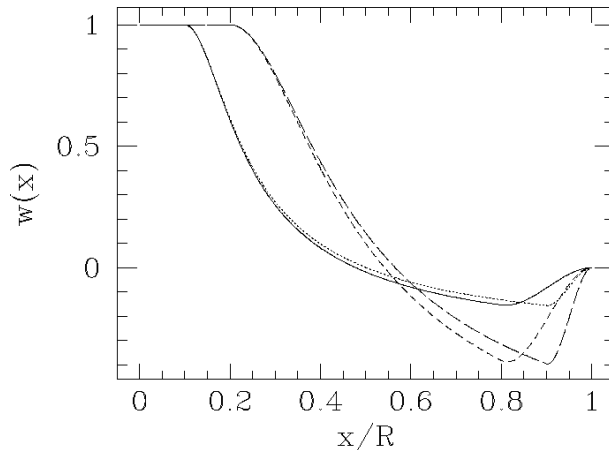


Fig. 1. The weight function $w(x)$ as defined in (34) as a function of x/R , for $(\nu_1, \nu_2) = (0.1, 0.8)$ (solid curve), $(0.1, 0.9)$ (dotted curve), $(0.2, 0.8)$ (short-dashed curve) and $(0.2, 0.9)$ (long-dashed curve)

The corresponding function $Q(x)$ can be calculated from (16); again, the resulting expressions are fairly cumbersome and shall not be reproduced here. For the same values of ν_1 and ν_2 as in Fig. 1, the corresponding function $Q(x)$ is plotted in Fig. 2.

Finally, the special case of a singular isothermal sphere is considered. In this case, $\langle \gamma_t \rangle = x_0/(2x)$, where

$$x_0 = 4\pi \left(\frac{\sigma_v}{c} \right)^2 \frac{D_{\text{ds}}}{D_s} \quad (35)$$

is the Einstein radius of the mass distribution. Using this tangential shear distribution in (28), one finds

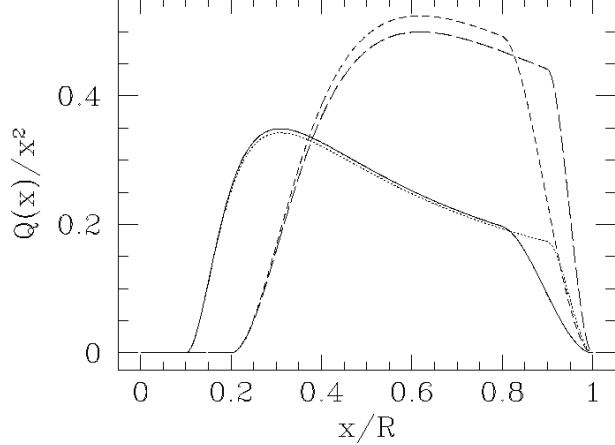


Fig. 2. For the same values of ν_1 and ν_2 as in Fig. 1, the corresponding function $Q(x)/x^2$ is plotted as a function of x/R . The identification of the curves is the same as in Fig. 1

$$S_c = \frac{\sqrt{\pi n x_0^2}}{\sigma_\epsilon} \frac{\int_0^R dx Q(x)/x^2}{\sqrt{\int_0^R dx Q^2(x)/x^3}} =: s \frac{\sqrt{\pi n x_0^2}}{\sigma_\epsilon} . \quad (36a)$$

Noting that the ratio of integrals does not depend on R for the function $Q(x)$ corresponding to $w(x)$ in (34), we have the remarkable fact that the signal-to-noise for a singular isothermal sphere is independent of the aperture size R , but depends only on *the expected number of galaxies within the Einstein radius x_0 and the intrinsic ellipticity dispersion of the sources*. For the weight function (18) defined by Kaiser, $Q = 0$ for $x \leq \nu_1 R = x_1$, and $Q = \text{const.}$ for $x \in [\nu_1 R, R]$. Also in this case does the ratio s of integrals not depend on R , and one can easily calculate that then $s = \sqrt{2(1 - \nu_1)/(1 + \nu_1)}$. The ratio s is plotted in Fig. 3 as a function of ν_1 , for $\nu_2 = 0.9$; in fact, the ratio s depends only weakly on ν_2 , as long as $(1 - \nu_2) \ll 1$. As can be seen, reducing ν_1 increases the signal-to-noise considerably for the weight function (34); for $\nu_1 \gtrsim 0.1$, the Kaiser weight function yields larger signal-to-noise ratios. This is due to the fact that for larger values of ν_1 , the weight function (34) deviates significantly from the optimal weight function (32). Since the choice (34) of w is by no means unique, one might try to construct functions which yield a higher signal-to-noise for ones favourite mass distribution. In this paper, we shall use w as given by (34), and restrict our attention to small values of ν_1 .

For reference, we rewrite (36a) in useful units as

$$S_c = 8.39 s \left(\frac{n}{30/\text{arcmin}^2} \right)^{1/2} \left(\frac{\sigma_v}{600 \text{km/s}} \right)^2 \left(\frac{\sigma_\epsilon}{0.2} \right)^{-1} \left(\frac{D_{\text{ds}}}{D_s} \right) . \quad (36b)$$

4 Detection of mass concentrations from synthetic data

In this section the finding of mass concentrations from the shear pattern in faint galaxy data is discussed. For this purpose, synthetic data are generated, which consist of a set of position vectors \mathbf{x}_i of galaxy images and their complex ellipticity ϵ_i . From these data,

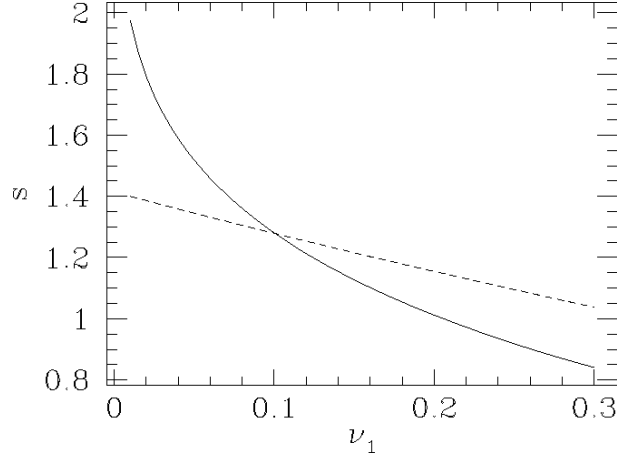


Fig. 3. The ratio s as defined in (36a), as a function of ν_1 . The solid curve is for the weight function $w(x)$ as defined in (34), for $\nu_2 = 0.9$, whereas the dashed curve has been calculated for the weight function (18) as defined by Kaiser (1995)

a signal-to-noise map is obtained, by calculating the function $S(\mathbf{x})$ as defined in (24) on a grid. Mass concentrations should show up as significant peaks in the S -map.

Galaxies are distributed randomly on a square of side x_f ; assuming a number density of n , $N = nx_f^2$ galaxies are placed on this square. For each such galaxy, the intrinsic ellipticity $\epsilon^{(s)}$ is drawn from the distribution function

$$p_s(\epsilon^{(s)}) = \frac{1}{\pi\sigma_\epsilon^2(1 - e^{-1/\sigma_\epsilon^2})} e^{-|\epsilon^{(s)}|^2/\sigma_\epsilon^2} , \quad (37)$$

and the value $\sigma_\epsilon = 0.2$ is taken throughout this paper (see Seitz & Schneider 1996, and references therein). For a given lens model, the surface mass density $\kappa(\mathbf{x}_i)$ and the shear $\gamma(\mathbf{x}_i)$ is calculated at each galaxy position, and the ‘observed’ ellipticity ϵ_i is calculated from (19). By selecting the galaxy positions randomly on the observer’s sky, we have implicitly assumed that the magnification bias can be neglected, i.e., that the number counts of galaxies follows approximately the law $d\log N(m)/dm \propto 10^{\gamma m}$, with $\gamma \approx 0.4$. For a given filter size R , the S -statistics is calculated on a square of size $x_f - 2R$, to avoid boundary effects.

4.1 Lens-free S -statistics

We first consider the case that no lenses are present, i.e., that $\epsilon_i = \epsilon_i^{(s)}$. In this case one expects that the S -statistics (24) has a Gaussian probability distribution of unit width,

$$p(S) = \frac{1}{\sqrt{2\pi}} e^{-S^2/2} . \quad (38)$$

To verify this expectation, a simulation was carried out with $x_f = 60'$, a number density of $n = 30/\text{arcmin}^2$ (this value will be used throughout the rest of this paper), and a grid of 1500^2 points at which S was calculated. The resulting probability distribution $p(S)$ is plotted in Fig. 4, together with the Gaussian (38). As can be seen, the probability distribution of S follows the expected Gaussian curve within the numerical errors.

In addition, a modified S -statistics was calculated which uses $S' = m/\sigma_{mc}$ instead of $S = m/\sigma_{md}$. Whereas the former is slightly more faster to evaluate, since σ_{mc} is

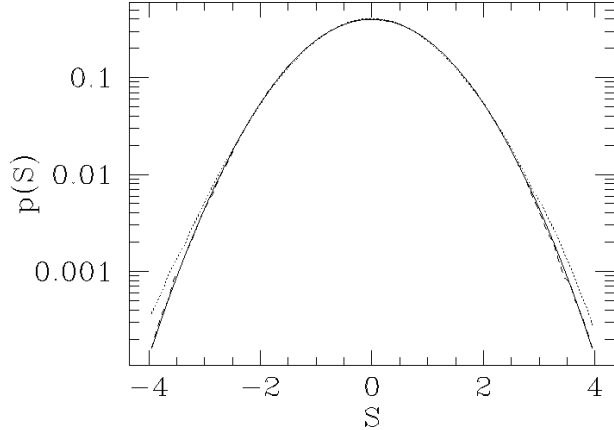


Fig. 4. The probability distribution $p(S)$ is plotted (dashed curve), together with the Gaussian distribution (38) (solid curve). Also, the distribution function for the S' statistics as defined in the text is plotted (dotted curve), which shows somewhat broader wings than the S -statistics. For these curves, $R = 0'5$ was used, with $\nu_1 = 0.1$ and $\nu_2 = 0.9$

independent of \mathbf{x}_0 , Fig. 4 shows that the probability distribution for S' has somewhat broader wings than that of S . The same simulations have been carried out with the weight function w_K , and the results are basically indistinguishable from those shown in Fig. 4.

To illustrate the spatial distribution of the function S , Fig. 5 displays contour maps of S on a square of sidelength $10'$; i.e., we have chosen $x_f = 10' + 2R$. No lensing has been assumed. Three different filter scales R are chosen in Fig. 5 for the weight function (34); in addition, an S -map for the filter w_K given in (18) has been plotted in the lower right panel. Obviously, by increasing R , the S -maps become smoother. It should be noted that the S -map for the w_K weight function is much ‘noisier’ than the one for the w weight function for the same filter size R (the two right-hand panels in Fig. 5). This is because the weight function w_K , and thus the corresponding function Q , are discontinuous, so that single galaxy images moving into the filter can cause sudden jumps of S . In the maps with small R , several peaks with $S > 3$ (or minima with $S < -3$) can be seen, but extrema with $|S| > 4$ are very rare, in accord with the result shown in Fig. 4.

4.2 Single-lens statistics

Next we study the statistical properties of the signal-to-noise S for a single isolated deflector. For this, a mass model is chosen which closely resembles an isothermal sphere with a finite core and a finite truncation radius, described by the (axially-symmetric) mass distribution

$$\kappa(x) = \frac{x_0}{2\sqrt{x^2 + x_c^2}} - \frac{x_0}{2\sqrt{x^2 + x_t^2}} \quad , \quad (39)$$

where x_c is the core radius, x_t the truncation radius, and x_0 is the Einstein angle of the corresponding singular isothermal model, given in (35). For the rest of the paper, a fixed value of $D_{\text{ds}}/D_s = 0.7$ is assumed. The (tangential) shear corresponding to this mass distribution is calculated as $\gamma \equiv \gamma_t = \bar{\kappa} - \kappa$, where

$$\bar{\kappa}(x) = \frac{x_0}{x^2} \left(\sqrt{x^2 + x_c^2} + x_t - \sqrt{x^2 + x_t^2} - x_c \right) \quad .$$

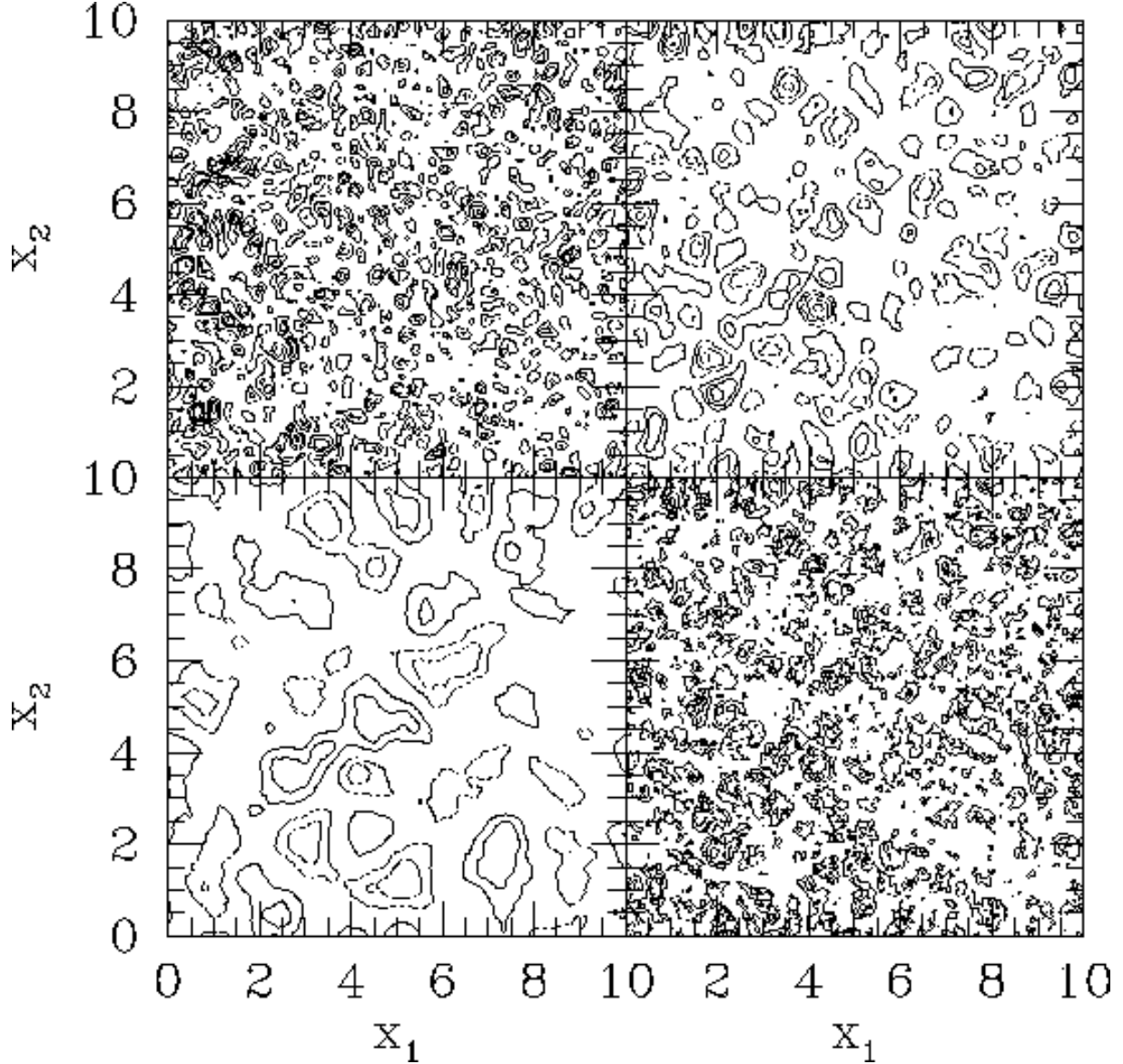


Fig. 5. Contour plots of the signal-to-noise ratio S defined in Eq. (24), for a surface number density of $n = 30/\text{arcmin}^2$, on a square of sidelength $10'$. No lensing has been assumed, i.e., the galaxy images are distributed randomly with an ellipticity distribution according to (37). In the upper left panel, $R = 0.5'$, in the upper right panel, $R = 1'$, and in the lower left panel, $R = 2'$. In these three cases, the weight function (34) was used, with $\nu_1 = 0.1$, $\nu_2 = 0.9$. The lower right panel uses the weight function w_K given in (18), for $R = 1'$ and $\nu_1 = x_1/R = 0.3$. Contour levels are $S = 1, 2, 3, \dots$ (solid contours) and $S = -1, -2, -3, \dots$ (dashed contours)

For this mass model, the expected signal-to-noise ratio S_c can be calculated from (28); for different values of σ_v and the ratio x_c/x_0 , this expected value is plotted as a function of the filter scale R in Fig. 6. In addition, simulations were made by distributing galaxies around these lenses with an intrinsic ellipticity distribution (37), then distorting them by the lens using (19), and calculating S according to (24) at the center of the lens, again for varying filter scale R . For different realizations of the galaxies, the resulting values of S are also plotted in Fig. 6.

Three different cases are shown in Fig. 6: for $x_c/x_0 = 1/3$, the lens is critical; it is nearly critical for $x_c/x_0 = 1$, and a rather weak lens for $x_c/x_0 = 3$. The ensemble-

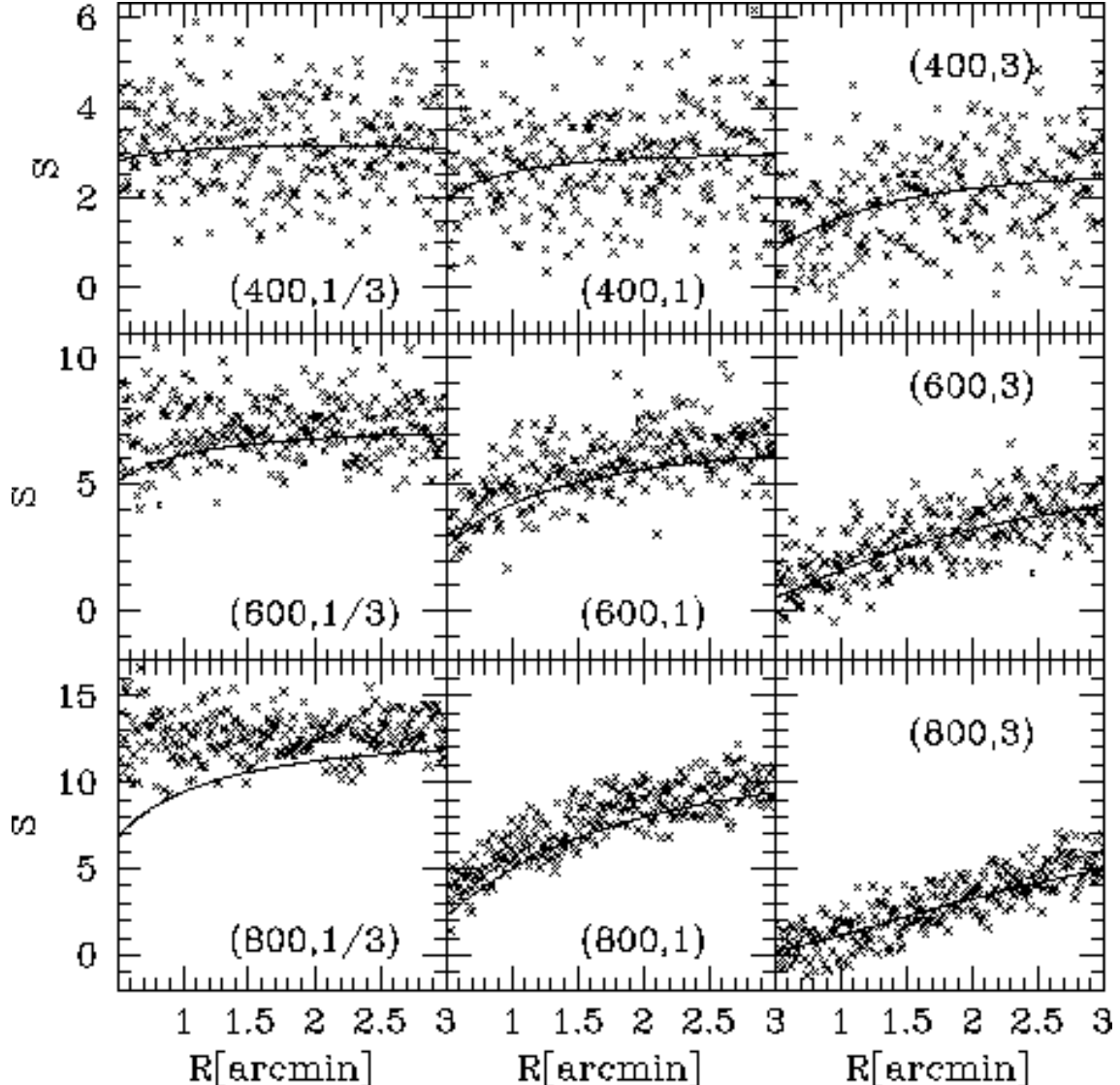


Fig. 6. The values of S – see Eq. (24) – for different realizations of the galaxy distribution and different filter radii R . The numbers in each panel shows the pair of values $(\sigma_v, x_c/x_0)$ (with σ_v in km/s) used in the lens model (39). The truncation radius is chosen to be $x_t = 50x_0$. For the weight function Q , the values $\nu_1 = 0.1$ and $\nu_2 = 0.9$ were chosen. The solid curve in each panel is the ensemble-averaged signal-to-noise S_c as given in (28). The systematic differences between the numerical results (crosses) and the analytic expectation are due to the non-linearity of the image distortion – see text

averaged signal-to-noise S_c as calculated from (28) lies well in the ‘middle’ of the numerically-generated points for the non-critical lens, but significantly underestimates S for the critical lenses. This is because the relation $g \approx \gamma$ – see (20) – is no longer valid near the center of a critical lens. In the calculation of (28) the true value of γ is used, whereas for calculating S according to (24), ϵ_t is used. Now, ϵ is an unbiased estimate for g , which is larger in magnitude than γ , so that S_c is biased toward lower values for strong or even critical lenses.

For critical lenses with $\sigma_v = 400$ km/s, the mean signal-to-noise is of order 3, as also follows from (36b). Hence, these lenses can be detected with a marginal significance, given the fact that S varies considerably around this expectation value for individual realizations. However, if the core radius becomes larger than about x_0 , these lenses are

too weak to be reliably discovered individually by the method proposed here. Lenses with $\sigma_v \gtrsim 600$ km/s can be discovered reliably if the core size is not too large. In addition to the core radius, the filter scale R plays an important role: if this filter scale is not considerably larger than the core radius, the S -statistics becomes very insensitive, since it measures radial gradients. Hence, if the filter has the same size as the core, no gradient can be measured. For critical lenses, even the smallest filter scale considered in Fig. 6 is sufficient, whereas for weak lenses with $x_c = 3x_0$, the filter scale R must be larger than 2.5 to detect reliably a lens with $\sigma_v = 800$ km/s. For such large core size, lenses with $\sigma_v = 600$ km/s are not reliably detected, but those with $x_c = x_0$ are if $R \gtrsim 1.5$. Note that the width of the distribution of points in all panels of Fig. 6 is of order unity.

4.3 S -statistics for an ensemble of lenses

Next we want to investigate whether the S -statistics is significantly degraded by not considering isolated lenses, but by studying an ensemble of lenses. Two kinds of effects may affect the S -statistics: small-scale mass concentrations which can locally dominate the shear field and which should increase the noise in the S -statistics, and larger-scale mass perturbations. The latter should not provide a problem for the detection of mass concentrations as long as their contribution can be described as a linear function across the size of the filter (i.e., where the weight function $Q(x)$ does not vanish). In order to study these effect, we have made simulations with rather extreme perturbations. Motivated by Fig. 6, it should be investigated whether lenses with the density profile (39) and with $\sigma_v = 600$ km/s and $x_c = x_0$ can be significantly detected; those will be called ‘main lenses’ in the following. They were distributed randomly with a number density of $16/\text{deg}^2$. In addition, small-scale lenses were added with $\sigma_v = 220$ km/s and $x_c = x_0$, and a density which is 100 times higher than that of the main lenses. To simulate larger-scale perturbations, lenses with $\sigma_v = 800$ km/s and $x_c = 5x_0$ were distributed with twice the density of the main lenses. Judging from Fig. 6, these ‘perturbing’ mass distributions should not be reliably identifiable in the S -map.

As can be seen from Fig. 7, several peaks occur with $S \gtrsim 5$, and all of them correspond to one of the ‘main lenses’; in fact, there is no single peak with $S \geq 5$ which is not located at a ‘main lens’ position. Some of the large-scale perturbing mass distributions, indicated by triangles in Fig. 7, produce local peaks with $3 \lesssim S \lesssim 5$, but these peaks cannot be confused with those corresponding to the ‘main deflectors’. From simulations of a larger angular field, the statistics of peaks – as shown in Fig. 8 – clearly indicates that all ‘main lenses’ are identified as $S \geq 5$ peaks, and none of the peaks with $S \geq 5$ is a ‘false detection’. We can thus conclude that the aperture method for the detection of matter concentrations does work not only for isolated axially-symmetric mass distributions, but also if one accounts for large- and small-scale ‘perturbations’ of the lens mapping.

4.4 Effects of a point-spread function

One of the most difficult problems for weak lensing studies from ground-based observations is the proper accounting for a point-spread function (PSF). The observed image ellipticity $\epsilon^{(\text{obs})}$ deviates from the true image ellipticity ϵ , depending on the size of the PSF and the size of the image. Small elliptical images are transformed into nearly round observed images by an isotropic PSF. In addition, anisotropies of the PSF can introduce spurious shear signals in the data. For these reasons, cluster-mass reconstructions

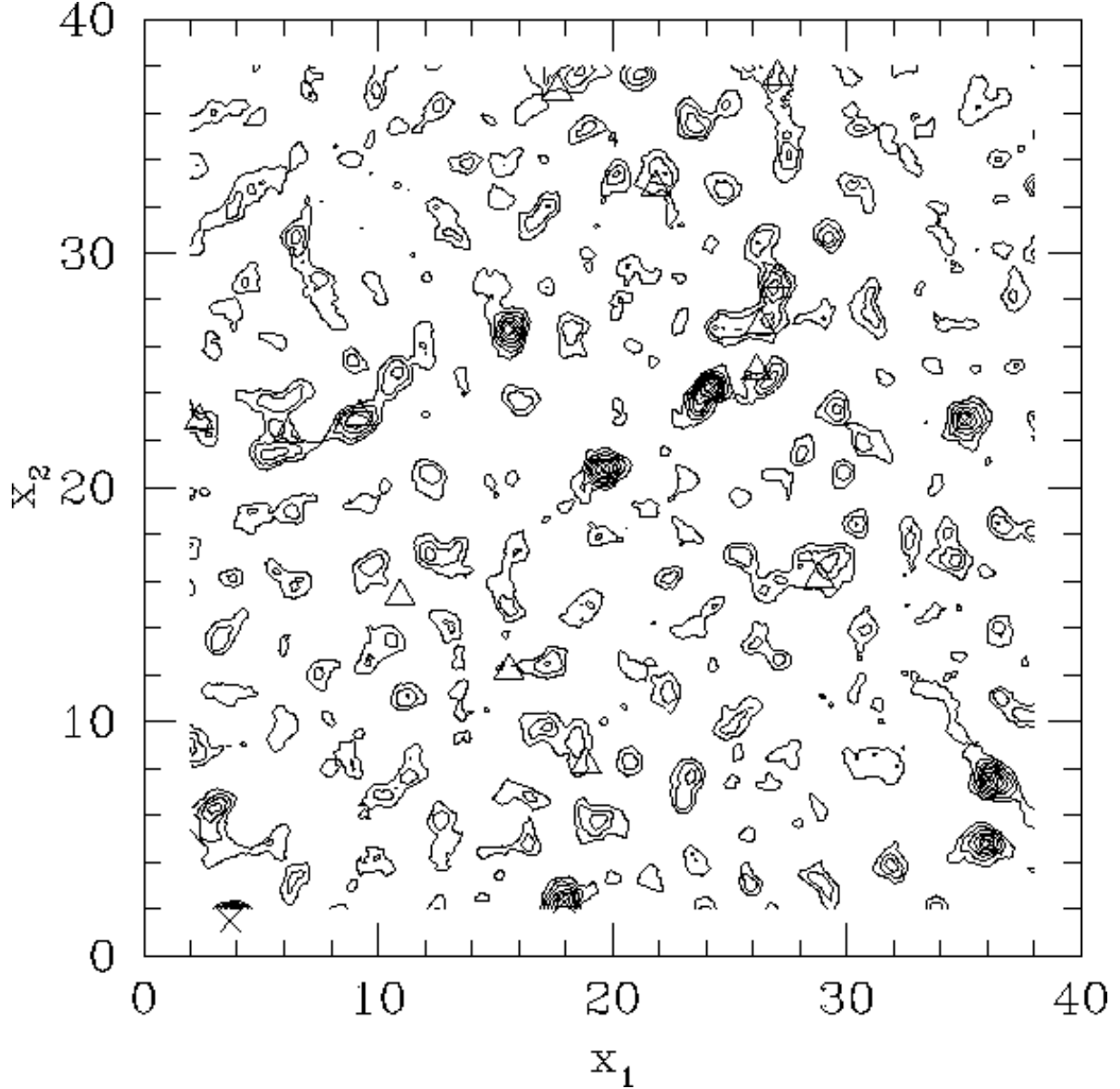


Fig. 7. A map of the S -statistics, with filter scale $R = 2'$, for the lens distribution as described in the text. Contours are $S = 1, 2, 3, \dots$, crosses denote the positions of the ‘main’ lenses with $\sigma_v = 600$ km/s and $x_c = x_0$, and triangles the position of the ‘perturbing’ lenses with $\sigma_v = 800$ km/s and $x_c = 5x_0$

from ground-based images have to correct for PSF effects (e.g., Bonnet & Mellier 1995; Kaiser, Squires & Broadhurst 1995). Depending on the seeing conditions, rather large correction factors have to be used to translate the ‘observed shear’ to the ‘true shear’. In this subsection, it will be demonstrated that PSF effects are much less important for the detection of dark matter concentrations if the method described before is applied.

In order to investigate the effects of a PSF on the observed image ellipticity, we note that the complex ellipticity is defined in terms of the second moment tensor Q_{ij} of the image brightness distribution as

$$\epsilon = \frac{Q_{11} - Q_{22} + 2iQ_{12}}{Q_{11} + Q_{22} + 2\sqrt{Q_{11}Q_{22} - Q_{12}^2}} \quad , \quad (40)$$

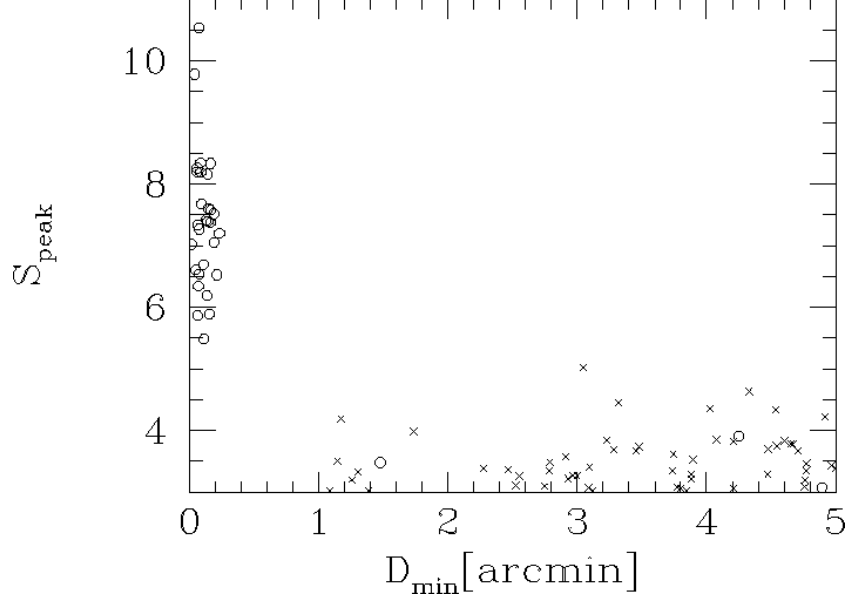


Fig. 8. Peak statistics: on a field with side $x_f = 80'$, lenses with $\sigma_v = 600 \text{ km/s}$ and $x_c = x_0$ (“main lenses”) were distributed with a density of $16/\text{deg}^2$; in addition, to simulate small-scale noise, hundred times as many lenses with $\sigma_v = 220 \text{ km/s}$ and $x_c = x_0$, and for simulating large-scale perturbations, two times as many lenses with $\sigma_v = 800 \text{ km/s}$ and $x_c = 5x_0$ were distributed. On the resulting S -map, all peaks with $S \geq 3$ were identified, and their separation D_{\min} to the nearest main lens was calculated. Plotted are the peaks of the S -map in the D_{\min} - S_{peak} plane. Circles corresponds to those peaks which are the closest ones to a main lens, and crosses denote the others. Here, a filter scale of $R = 2'$ was used. All peaks with $S_{\text{peak}} \geq 5$ are situated within $R/7$ from a main lens; hence, all peaks with $S_{\text{peak}} \gtrsim 5$ correspond to a mass concentration. Of the 29 main lenses in the field, the lowest one has $S_{\text{peak}} = 5.36$, three have $S_{\text{peak}} \in [5, 6]$, nine have $S_{\text{peak}} \in [6, 7]$, 13 have $S_{\text{peak}} \in [7, 8]$, and the other four main lenses have $S_{\text{peak}} \geq 8$. Thus, not only are there no false detections of main lenses for $S_{\text{peak}} \geq 5$, but also all the main lenses are detected with $S_{\text{peak}} \geq 5$

where

$$Q_{ij} = \frac{\int d^2x I(\mathbf{x}) (x_i - \bar{x}_i)(x_j - \bar{x}_j)}{\int d^2x I(\mathbf{x})} \quad , \quad (41a)$$

and $\bar{\mathbf{x}}$ is the ‘center’ of the image,

$$\bar{\mathbf{x}} = \frac{\int d^2x I(\mathbf{x}) \mathbf{x}}{\int d^2x I(\mathbf{x})} \quad . \quad (41b)$$

In a similar way, we define the complex ellipticity $\epsilon^{(\text{obs})}$ in terms of the second moment tensor $Q_{ij}^{(\text{obs})}$, which is defined in terms of the observed brightness profile

$$I^{(\text{obs})}(\mathbf{xx}) = \int d^2y I(\mathbf{y}) P(\mathbf{x} - \mathbf{y}) \quad , \quad (42)$$

where $P(\mathbf{x})$ is the PSF, which is assumed to be normalized. From these relations, one finds that the relation between Q_{ij} and $Q_{ij}^{(\text{obs})}$ reads

$$Q_{ij}^{(\text{obs})} = Q_{ij} + P_{ij} \quad , \quad (43)$$

where

$$P_{ij} = \int d^2z P(\mathbf{z}) (z_i - \bar{z}_i)(z_j - \bar{z}_j) \quad , \quad (44a)$$

and

$$\bar{\mathbf{z}} = \int d^2 z P(\mathbf{z}) \mathbf{z} \quad . \quad (44b)$$

From these relations, one can obtain $\epsilon^{(\text{obs})}$ in dependence of ϵ . A slightly more convenient way to find this relation is to consider the ellipticity variable

$$\chi = \frac{Q_{11} - Q_{22} + 2iQ_{12}}{Q_{11} + Q_{22}} = \frac{2\epsilon}{1 + |\epsilon|^2} \quad , \quad (45)$$

and correspondingly for $\chi^{(\text{obs})}$. Then, in agreement with a similar result derived in Bartelmann (1995) and Villumsen (1995),

$$\chi^{(\text{obs})} = \frac{\chi + T\chi^{(\text{PSF})}}{1 + T} \quad , \quad (46)$$

where T describes the ratio of the size of the PSF and the size of the image, and $\chi^{(\text{PSF})}$ accounts for a possible anisotropy of the PSF,

$$T = \frac{P_{11} + P_{22}}{Q_{11} + Q_{22}} ; \quad \chi^{(\text{PSF})} = \frac{P_{11} - P_{22} + 2iP_{12}}{P_{11} + P_{22}} \quad . \quad (47)$$

Hence, (46) expresses the fact that for small T (i.e., size of the PSF small compared to the image size), the observed ellipticity is approximately equal to the true ellipticity of the image, whereas for large T , the observed ellipticity can be dominated by the ellipticity of the PSF. Using the inverse of (45),

$$\epsilon = \frac{\chi}{1 + \sqrt{1 - |\chi|^2}} \quad , \quad (48)$$

one can now calculate $\epsilon^{(\text{obs})}$ as a function of ϵ , for a given PSF and for a given image size. We define the size θ of an image, and the size σ of the seeing disk as

$$\theta := \sqrt{Q_{11} + Q_{22}} \quad ; \quad \sigma^2 = P_{11} + P_{22} \quad , \quad (49)$$

so that $T = \sigma^2/\theta^2$.

As in the idealized case of negligible seeing, we define in analogy to (22)

$$m^{(\text{obs})}(\mathbf{x}_0) = \frac{1}{n} \sum_i \frac{\epsilon_{ti}^{(\text{obs})}(\mathbf{x}_0)}{|\mathbf{x}_i - \mathbf{x}_0|^2} Q(|\mathbf{x}_i - \mathbf{x}_0|) \quad . \quad (50)$$

Whereas $m^{(\text{obs})}$ will deviate significantly from m due to seeing effects, and thus no longer is an approximation for the w -weighted mass density as defined in (9), one can still use $m^{(\text{obs})}$ to measure local mass overdensities; in particular, one can in analogy to (24) define the signal-to-noise ratio

$$S^{(\text{obs})}(\mathbf{x}_0) = \frac{\sqrt{2}}{\sigma_{\epsilon}^{(\text{obs})}} \frac{\sum_i \frac{\epsilon_{ti}^{(\text{obs})}(\mathbf{x}_0)}{|\mathbf{x}_i - \mathbf{x}_0|^2} Q(|\mathbf{x}_i - \mathbf{x}_0|)}{\sqrt{\sum_i \frac{Q^2(|\mathbf{x}_i - \mathbf{x}_0|)}{|\mathbf{x}_i - \mathbf{x}_0|^4}}} \quad , \quad (51)$$

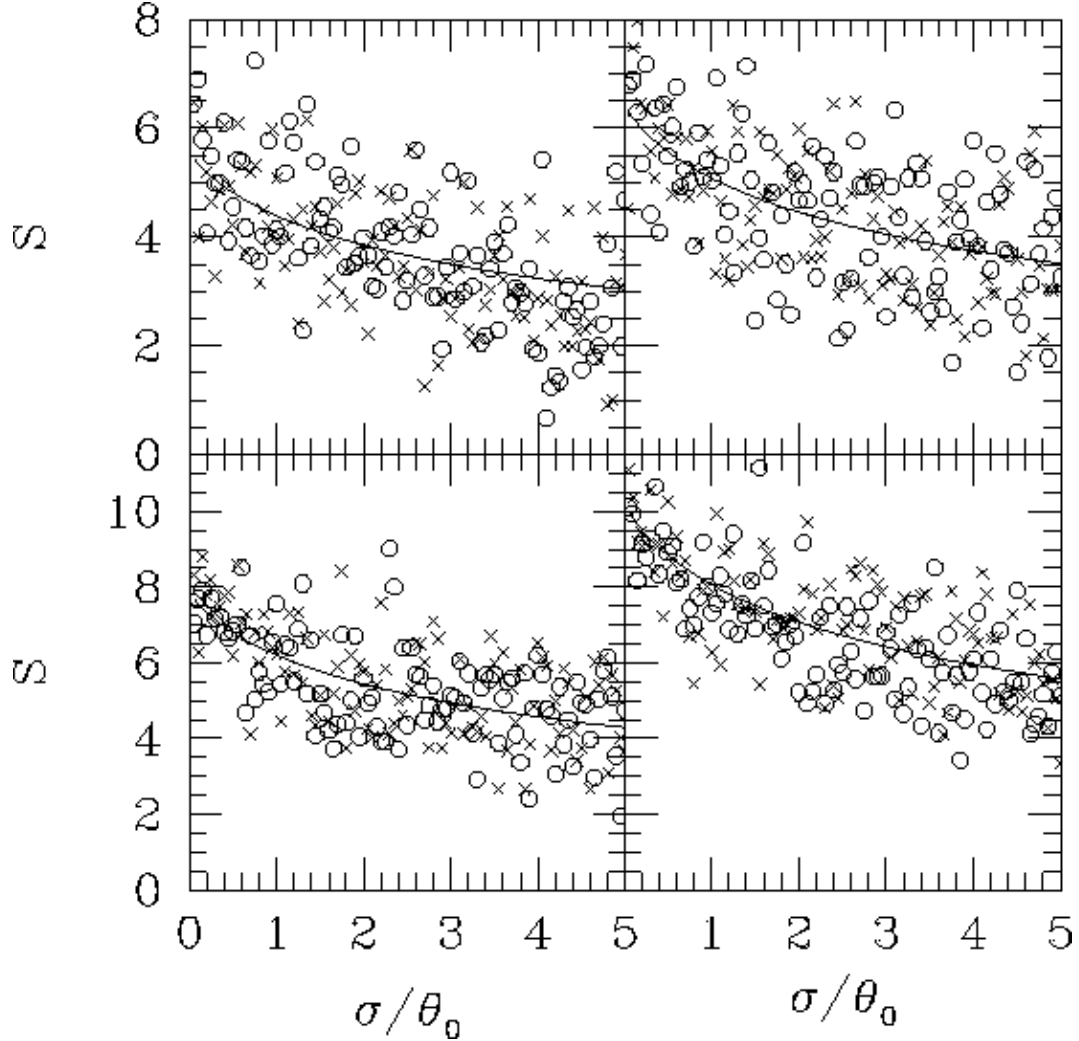


Fig. 9. The signal-to-noise ratio $S^{(\text{obs})}$ as a function of the ratio of the size σ of the seeing disk and the characteristic size θ_0 of the galaxy distribution. Here, the size distribution (54a) was assumed. An ‘isothermal’ lens model of the form (39) was assumed, with $x_c = x_0$ and $x_t = 50x_0$. In the upper panels, $\sigma_v = 600$ km/s, in the lower panels, $\sigma_v = 800$ km/s. The filter size R in the two left panels is $R = 1.5'$, and $R = 3'$ in the right panels. The value of $S^{(\text{obs})}$ is plotted as crosses for an isotropic PSF (i.e., $\chi^{(\text{PSF})} = 0$), whereas the circles show the values for a PSF with $\chi^{(\text{PSF})} = 0.1$. As in the rest of this paper, the number density of galaxy images was taken to be $30/\text{sq. arcmin}$. The solid curve displays the ensemble-averaged signal-to-noise ratio, $\langle m^{(\text{obs})} \rangle / \sigma_{mc}$, calculated for an isotropic PSF

where $\sigma_e^{(\text{obs})}$ is the dispersion of the *observed* ellipticities. Hence, whereas the ‘signal’ $m^{(\text{obs})}$ will be smaller due to seeing than m , so will be the dispersion, and one might expect that the signal-to-noise ratio is not as badly affected as the signal itself.

For an assumed size distribution $p_\theta(\theta)$ of the images, one can define the expectation value of $m^{(\text{obs})}$ for the center of an axially-symmetric mass distribution (again, we shall drop the argument \mathbf{x}_0 in the following) as

$$\begin{aligned}
\langle m^{(\text{obs})} \rangle &= \frac{1}{n} \left[\prod_{k=1}^N \int d\theta_k p_\theta(\theta_k) \int d^2 \epsilon_k^{(\text{s})} p_s(\epsilon_k^{(\text{s})}) \int \frac{d^2 x_k}{\pi R^2} \right] m^{(\text{obs})} \\
&= 2\pi \int d\theta p_\theta(\theta) \int d^2 \epsilon^{(\text{s})} p_s(\epsilon^{(\text{s})}) \int_0^R dx \frac{\epsilon_t^{(\text{obs})} Q(x)}{x} .
\end{aligned} \tag{52}$$

Note that in this equation, $\epsilon_t^{(\text{obs})}$ is a function of $\epsilon^{(\text{s})}$ and the reduced shear $g(x)$ through (19), i.e., to determine the true image ellipticity ϵ , and of θ (and the PSF) through the transformation (45), (46) and (48) from ϵ to $\epsilon^{(\text{obs})}$. Because of the delicate dependencies, no further analytic progress can be made, and (52) has to be evaluated numerically. Similarly, one can calculate the dispersion of $m^{(\text{obs})}$ in the absence of a lens,

$$\sigma_{mc}^2 = \frac{2\pi}{n} \int d\theta p_\theta(\theta) \int d^2 \epsilon^{(\text{s})} p_s(\epsilon^{(\text{s})}) (\epsilon_t^{(\text{obs})})^2 \int_0^R \frac{dx Q^2(x)}{x^3} . \tag{53}$$

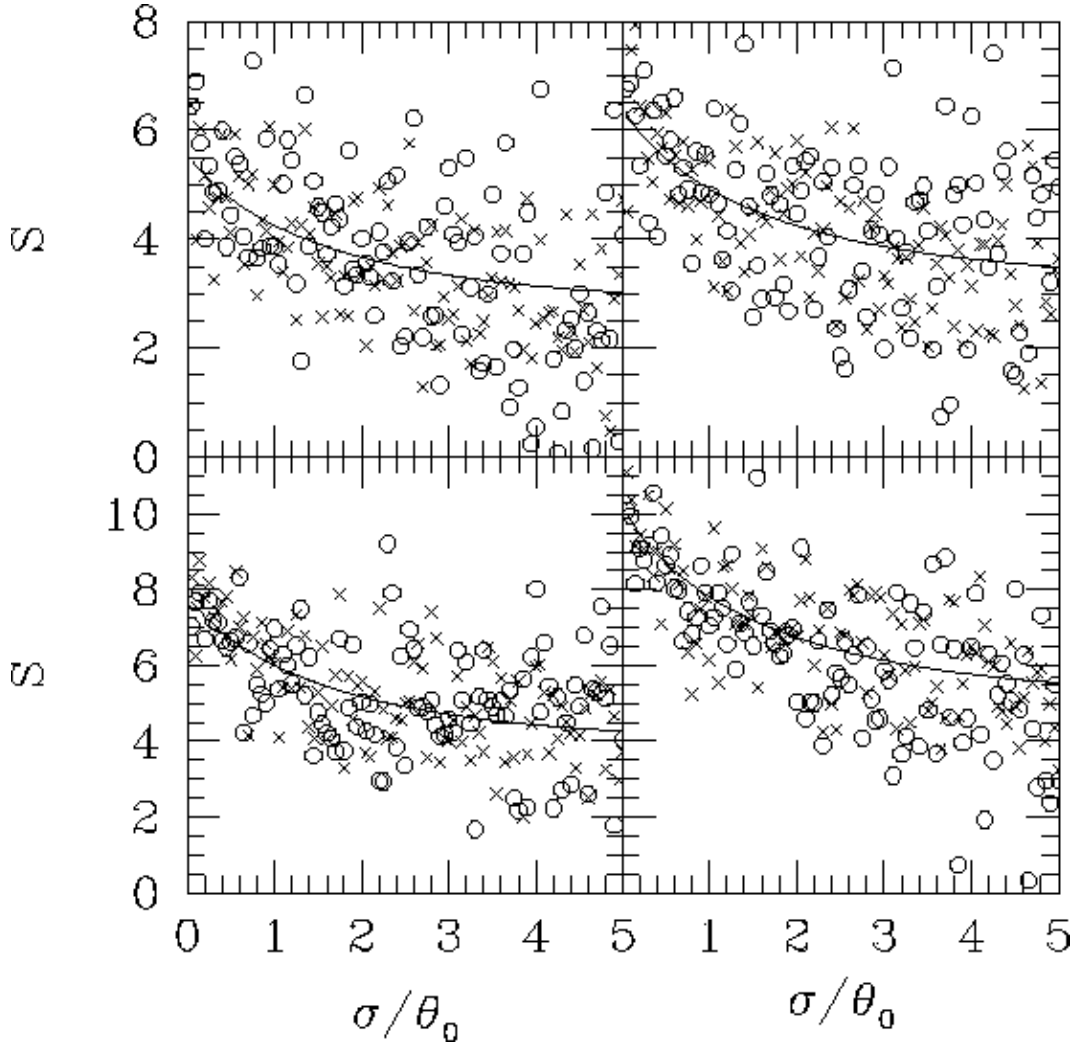


Fig. 10. Same as Fig. 9, except that now the size distribution (54b) instead of (54a) was used

For the lens model described by (39), we have calculated the ensemble-averaged signal-to-noise, $S_c = \langle m^{(\text{obs})} \rangle / \sigma_{mc}$, according to (52) and (53) for an isotropic PSF, and $S^{(\text{obs})}$ for different realizations of the galaxy distribution, as a function of the ratio σ/θ_0 , where θ_0 characterizes the size distribution of the galaxy images. In particular, we have chosen the following two distributions:

$$p_\theta(\theta) = \frac{\theta_0}{(\theta + \theta_0)^2} , \quad (54a)$$

or

$$p_\theta(\theta) = \frac{1}{\theta_0} e^{-\theta/\theta_0} . \quad (54b)$$

It is obvious that S depends only on the ratio σ/θ_0 , since there are no other relevant scales in the problem. The results of these calculations are shown in Fig. 9 for the distribution function (54a), and in Fig. 10 for the distribution function (54b).

The symbols in Figs. 9 and 10 show $S^{(\text{obs})}$ for different realizations of the background galaxy population, calculated from (51), whereas the solid curve shows $S_c = \langle m^{(\text{obs})} \rangle / \sigma_{mc}$, for two values of the velocity dispersion σ_v and two values for the filter size R . Crosses denote values of $S^{(\text{obs})}$ calculated for an isotropic PSF, whereas the circles assume that the PSF is anisotropic, characterized by $\chi^{(\text{PSF})} = 0.1$. As can be seen, most clearly from Fig. 10, the distribution of the circles is broader relative to that of the crosses; this is due to the fact that for an anisotropic PSF, the contribution of a galaxy image to the sum in the numerator of (51) does not only depend on the radial separation of the image from the point of interest, but also on its polar coordinate, since $\chi^{(\text{PSF})}$ enters ϵ_t as a term $\propto \cos(2\varphi)$. Hence, the polar coordinates of the galaxy images provides an additional source of ‘Poisson noise’ in $S^{(\text{obs})}$. The effect of a PSF is stronger for the size distribution (54b) than for (54a), for fixed θ_0 , which is due to the fact that for (54a) the number of ‘large’ sources is considerably larger than for (54b). As can be inferred from the figures, lenses with $\sigma_v = 600$ km/s can still be reliably detected if the seeing is not much larger than the characteristic size θ_0 of the galaxy distribution. However, even for $\sigma \lesssim 5\theta_0$ can lenses with $\sigma_v = 800$ km/s be discovered, independent of whether the PSF is isotropic or not. Thus we see that the effect of a PSF is much less dramatic than might have been expected. This is mainly due to the fact that not only the signal is weakened by a PSF, but also the noise, so that the signal-to-noise ratio is much more weakly affected by a PSF than the signal alone.

5 Discussion

The aperture densitometry (1) developed by Kaiser (1995) has been generalized in this paper to arbitrary weight functions w in (9). Whereas the resulting aperture mass measure (9) then no longer has such an intuitive meaning as (1), this generalization allows the definition of a measure which yields the highest signal-to-noise for the detection of mass concentrations with an assumed radial profile. In addition, by choosing w appropriately, one can construct a smooth signal-to-noise map from an observed image. The weight function (34) used throughout this paper was constructed by assuming the dark matter concentrations to have approximately an isothermal profile. Numerical simulations have then shown that dark matter halos can be detected reliably provided their typical

velocity dispersion exceeds about 600 km/s (for an assumed density of galaxy images of $30/\text{arcmin}^2$, typical of current deep images from 4-m class telescopes); inclusion of seeing slightly weakens the lensing signal, and, depending on the ratio of the size of the seeing disk and the characteristic image size of faint background galaxies, slightly more massive mass concentrations are necessary for a robust detection. Even a significant anisotropy of the PSF does not seriously affect the signal-to-noise ratio as long as the PSF is roughly constant across the filter scale R .

The main advantage of the method proposed here is that the signal-to-noise can be directly estimated from the data and thus allows the determination of a significance level from the data only. In addition, it can be easily calculated from a list of galaxy images which contains positions and image ellipticities. For these reasons, a signal-to-noise map can be routinely constructed for all sufficiently deep wide-field images with good imaging quality. Since wide-field cameras will become increasingly available, this method will allow to perform a survey of mass concentrations selected by mass only (in contrast to light)! A mass-selected sample of dark halos is much more closely related to theories of structure formation in the universe and can be directly compared with numerical simulations, whereas optical or X-ray-selected samples of dark halos can be compared with the results of numerical simulations of structure formation only with additional assumptions concerning star formation histories and efficiencies, feed-back processes (e.g., from supernova explosions), or gas-dynamical processes. Results from lensing in clusters like MS 1224 (Fahlman et al. 1994) and Cl0939+4713 (Seitz et al. 1996) have yielded quite a broad range of mass-to-light ratios, which implies that by ‘radiation-selected’ samples of dark halos those with low mass-to-light ratios will be preferentially included.

A first attempt to discover dark matter concentrations by weak lensing has been successfully made by Fort et al. (1996) by investigating the shear field around high-redshift bright QSOs which are suspected to be affected by the magnification bias. The method presented in this paper will allow to extend the search for dark matter halos to a much larger angular region on the sky.

Further improvements of the detection method are possible. For example, in Sect. 4.4 the effects of a PSF were not included in the S -statistics explicitly, i.e., not attempt for correcting the image ellipticities for a PSF was made. If the PSF is known and stable over the filter size R , one can define in analogy to (50) an aperture measure $m^{(\text{obs})}$ in which the sum over the images is weighted according to the size of the images; large images contribute a larger signal than smaller images. The weights can again be optimized to yield the largest signal-to-noise ratio. In addition, the detection of weak shear from the surface brightness autocorrelation function (Van Waerbeke et al. 1996) provides an alternative and completely independent means for measuring the shear. This will be the subject of a future publication.

This work was supported by the ‘‘Sonderforschungsbereich 375-95 für Astro-Teilchenphysik’’ der Deutschen Forschungsgemeinschaft.

References

Bartelmann, M. 1995, A&A 303, 643.
 Bartelmann, M., Narayan, R., Seitz, S. & Schneider, P. 1995, ApJ (submitted).
 Bartelmann, M. & Schneider, P. 1993, A&A 271, 421.

Bartelmann, M. & Schneider, P. 1994, A&A 284, 1.

Benitez, N. & Martinez-Gonzalez, E. 1995, ApJ 448, L89.

Bonnet, H. & Mellier, Y. 1995, A&A 303, 331.

Dalcanton, J.J., Canizares, C.R., Granados, A., Steidel, C.C. & Stocke, J.T. 1994, ApJ 424, 550.

Fahlman, G., Kaiser, N., Squires, G. & Woods, D. 1994, ApJ 437, 56.

Fort, B. & Mellier, Y. 1994, A&AR 5, 239.

Fort, B., Mellier, Y., Dantel-Fort, M., Bonnet, H. & Kneib, J.-P. 1996, A&A, in press.

Fugmann, W. 1990, A&A 240, 11.

Hutchings, J.B. 1995, AJ 109, 928.

Kaiser, N. 1995, ApJ 439, L1.

Kaiser, N. & Squires, G. 1993, ApJ 404, 441.

Kaiser, N., Squires, G. & Broadhurst, T. 1995, ApJ 449, 460.

Kochanek, C.S. 1993, ApJ 419, 12.

Kochanek, C.S. 1995b, preprint (astro-ph/9510077).

Maoz, D. & Rix, H.-W. 1993, ApJ 416, 425.

Miralda-Escudé, J. & Babul, A. 1995, ApJ 449, 18.

Rodrigues-Williams, L.L. & Hogan, C.J. 1994, AJ 107, 451.

Schneider, P. 1993, A&A 279, 1.

Schneider, P. 1995, A&A 302, 639.

Schneider, P., Ehlers, J. & Falco, E.E. 1992, *Gravitational lenses*, Springer: New York (SEF).

Schneider, P. & Seitz, C. 1995, A&A 294, 411.

Schramm, T. & Kayser, R. 1995, A&A 299, 1.

Seitz, C. & Schneider, P. 1995a, A&A 297, 287.

Seitz, C. & Schneider, P. 1996a, A&A (submitted).

Seitz, C., Kneib, J.-P., Schneider, P. & Seitz, S. 1996, A&A (submitted).

Seitz, S. & Schneider, P. 1995b, A&A 302, 9.

Seitz, S. & Schneider, P. 1996b, A&A, in press.

Squires, G. & Kaiser, N. 1996, ApJ (submitted).

Tyson, J.A., Valdes, F. & Wenk, R.A. 1990, ApJ 349, L1.

Van Waerbeke, L., Mellier, Y., Schneider, P., Fort, B. & Mathez, G. 1996, in preparation.

Villumsen, J.V. 1995, MNRAS, submitted.